

# DIVERSE CHEMO-DYNAMICAL PROPERTIES OF NITROGEN-RICH STARS IDENTIFIED FROM LOW-RESOLUTION SPECTRA

CHANGMIN KIM<sup>1</sup>, YOUNG SUN LEE<sup>2,3</sup>, TIMOTHY C. BEERS<sup>3</sup>, AND YOUNG KWANG KIM<sup>2</sup>

<sup>1</sup>Department of Astronomy, Space Science and Geology, Chungnam National University, Daejeon 34134, Korea

<sup>2</sup>Department of Astronomy and Space Science, Chungnam National University, Daejeon 34134, Korea

<sup>3</sup>Department of Physics and Astronomy and JINA Center for the Evolution of the Elements, University of Notre Dame, IN 46556, USA

Received ; accepted

**Abstract:** The second generation of stars in the globular clusters (GCs) of the Milky Way (MW) exhibit unusually high N, Na, or Al, compared to typical Galactic halo stars at similar metallicities. The halo field stars enhanced with such elements are believed to have originated in disrupted GCs or escaped from existing GCs. We identify such stars in the metallicity range  $-3.0 < [\text{Fe}/\text{H}] < 0.0$  from a sample of  $\sim 36,800$  giant stars observed in the Sloan Digital Sky Survey and Large Sky Area Multi-Object Fiber Spectroscopic Telescope survey, and present their dynamical properties. The N-rich population (NRP) and N-normal population (NNP) among our giant sample do not exhibit similarities in either in their metallicity distribution function (MDF) or dynamical properties. We find that, even though the MDF of the NRP looks similar to that of the MW's GCs in the range of  $[\text{Fe}/\text{H}] < -1.0$ , our analysis of the dynamical properties does not indicate similarities between them in the same metallicity range, implying that the escaped members from existing GCs may account for a small fraction of our N-rich stars, or the orbits of the present GCs have been altered by the dynamical friction of the MW. We also find a significant increase in the fraction of N-rich stars in the halo field in the very metal-poor (VMP;  $[\text{Fe}/\text{H}] < -2.0$ ) regime, comprising up to  $\sim 20\%$  of the fraction of the N-rich stars below  $[\text{Fe}/\text{H}] = -2.5$ , hinting that partially or fully destroyed VMP GCs may have in some degree contributed to the Galactic halo. A more detailed dynamical analysis of the NRP reveals that our sample of N-rich stars do not share a single common origin. Although a substantial fraction of the N-rich stars seem to originate from the GCs formed in situ, more than 60% of them are not associated with those of typical Galactic populations, but probably have extragalactic origins associated with Gaia Sausage/Enceladus, Sequoia, and Sagittarius dwarf galaxies, as well as with presently unrecognized progenitors.

**Key words:** Method: data analysis – technique: spectroscopy – Galaxy: halo – stars: abundances

## 1. INTRODUCTION

The Milky Way (MW) hosts about 170 globular clusters (GCs) (e.g., Gratton et al. 2004; Baumgardt & Vasiliev 2021; Vasiliev & Baumgardt 2021, and references therein). Most GCs are known to exhibit signatures of multiple stellar populations (e.g., Carretta et al. 2009, 2010; Milone et al. 2015; Piotto et al. 2015), which are generally divided into two groups of stars according to differences in their individual elemental abundances: first-generation (FG) and second-generation (SG) stars. Numerous spectroscopic studies of GCs have revealed that the FG stars in GCs overall follow the chemical-abundance patterns of the Galactic field stars at similar metallicities. On the contrary, the SG stars exhibit enhancements of N, Na, and Al, while C, O, and Mg are depleted (see Bastian & Lardo 2018 for a detailed review), establishing anti-correlations between C and N, O and Na, and Mg and Al (Carretta et al. 2009, 2010; Carretta 2016; Martell et al. 2016; Tang et al. 2020; Horta et al. 2021).

A large number of chemical-abundance studies have reported that some fraction of the Galactic halo stars exhibit anomalous abundances of these same elements (Carretta et al. 2010; Fernández-Trincado et al. 2016; Martell et al. 2016; Pereira et al. 2019), as well as enhancements of slow neutron-capture elements (e.g., Majewski et al. 2012; Hasselquist et al. 2016; Pereira et al. 2017), which are characteristics frequently observed among the SG stars in GCs (Carretta et al. 2009; Carretta 2016; Pancino et al. 2017; Schiavon et al. 2017a; Tang et al. 2021; Fernández-Trincado et al. 2022). These studies argued for a possible connection in terms of their origin between the SG stars and field halo stars with large enhancements of N, Na, or Al. Such field stars are now believed to have originated from tidally disrupted GCs (Carretta et al. 2009, 2010; Carretta 2016; Fernández-Trincado et al. 2016, 2017, 2019, 2022; Martell et al. 2016; Schiavon et al. 2017a; Horta et al. 2021; Tang et al. 2021). A recent study of the tidally disrupting GC Palomar 5 finds N-rich stars both within and beyond its tidal radius, strongly supporting the idea that the stars enhanced with N, Na, or Al in the Galactic halo field have GC origins (Phillips et al.

CORRESPONDING AUTHOR: Young Sun Lee (young-sun@cnu.ac.kr)

2022).

The existence of such stars in the halo has profound implications on the assembly history of the MW, as GCs could contribute significantly to building up the baryonic mass of the MW (Carretta et al. 2010; Martell et al. 2016; Schiavon et al. 2017a; Lee et al. 2019; Hughes et al. 2020; Thomas et al. 2020; Wan et al. 2020; Lim et al. 2021), through their dissolution and/or evaporation (e.g., Elmegreen & Hunter 2010; Kruijssen et al. 2011). Consequently, understanding the fraction and nature of stars associated with the disrupted population from the GCs can provide important constraints on models for the assembly history of the MW. Among the stars with the GC origin, the abundance patterns of the FG stars are indistinguishable from the field halo stellar population, hence stars with the chemical abundances of the SG stars are used as tracers of the members of dissolved GCs. That is, while the SG stars reveal that partially or totally disrupted GCs have contributed to the halo, there are *also* the FG stars that have contributed, but are not readily identifiable.

Upon recognizing their importance, using the abundances of N, Na, or Al from various spectroscopic survey data, such as the Sloan Extension for Galactic Understanding and Exploration (SEGUE; Yanny et al. 2009; Rockosi et al. 2022), the Apache Point Observatory Galactic Evolution Experiment (APOGEE; Majewski et al. 2017), and the Large Sky Area Multi-Object Fiber Spectroscopic Telescope (LAMOST; Cui et al. 2012), numerous studies have attempted to discover examples of stars that were once GC members, but have been stripped from their progenitors (Martell & Grebel 2010; Martell et al. 2016; Fernández-Trincado et al. 2016, 2017, 2019, 2022; Schiavon et al. 2017a; Koch et al. 2019; Hanke et al. 2020; Horta et al. 2021; Kisku et al. 2021), in order to estimate their contribution to the mass assembly of the MW halo. These studies predicted fractions of 2 – 28% of SG stars originating in GCs, depending on the spatial extent explored in the surveys. Their contribution appears to become larger in the Galactic bulge than the halo (Schiavon et al. 2017a; Horta et al. 2021). These results confirm that stars with GC origins are one source of stellar constituents of the Galactic halo and bulge populations, indicating that the GCs must have played a role in the assembly of the MW.

The GCs in the MW originated from two different paths: in situ and ex situ. The ex situ (or accreted) channel consists of GCs that once belonged to dwarf galaxies which were accreted by the MW (e.g., Pfeffer et al. 2019; Hughes et al. 2020). The in situ path produces GCs that are thought to have formed in the turbulent disk of the MW at redshifts of  $z \sim 2 - 3$  (e.g., Kruijssen et al. 2012). This implies that the GC-origin stars not only came from GCs that formed in situ, but also those accreted from dwarf satellites (Fernández-Trincado et al. 2020b, 2021a). A recent study used the APOGEE data in the Sloan Digital Sky Survey (SDSS; York et al. 2000) Data Release 17 (DR17; Abdurro'uf et al. 2022) to identify 149 N-rich ( $[N/Fe] \geq +0.5$ ) red giants with

$[C/Fe] < +0.15$  in the metallicity range  $-1.8 < [Fe/H] < -0.7$ , combined with previously identified N-rich stars, to construct a catalog of 412 unique N-enhanced stars (Fernández-Trincado et al. 2022). These authors carried out a dynamical analysis of the compiled N-rich stars, and found that their origins are diverse; some may be dissolved members of GCs, which were brought into the MW during major merger events such as the Gaia-Sausage/Enceladus (GSE; Belokurov et al. 2018; Helmi et al. 2018). This indicates that extragalactic GCs may take part in the assembly of the MW as well.

Despite enormous progress in recent years, the identified chemically peculiar field stars presumably formed in GCs are not sufficiently numerous to closely examine their diverse origins. Furthermore, most previous studies focused on the narrow range of the metallicity ( $-2.0 < [Fe/H] < -1.0$ ). The identification of many more such stars, covering a wider metallicity range, is clearly desirable, and will provide a more clear picture on their role in the assembly of the MW. In this regard, low-resolution spectroscopic surveys such as SDSS and LAMOST, which provide a large dataset are excellent sources for conducting searches for N-rich stars over a wide range of metallicity and luminosity, compared to high-resolution spectroscopic data, which are best suited for detailed analyses of their chemical elements. This study presents a sample of N-rich stars identified from SDSS and LAMOST, and carries out an analysis of their dynamical properties in order to explore the diverse origins of their host systems.

The outline of this paper is as follows. In Section 2, we describe how we select the N-rich stars, followed by calculations of the space velocities and orbital parameters in Section 3. We present our findings and discuss their implications, along with those of previous studies, in Section 4. Section 5 summarizes our conclusions.

## 2. SELECTION OF NITROGEN-RICH STARS

To identify N-rich stars from the SDSS and LAMOST surveys, we first need to determine stellar parameters ( $T_{\text{eff}}$ ,  $\log g$ , and  $[Fe/H]$ ). We applied the SEGUE Stellar Parameter Pipeline (SSPP; Allende Prieto et al. 2008; Lee et al. 2008a,b, 2011a; Smolinski et al. 2011; Lee et al. 2013) to low-resolution spectra from SDSS and LAMOST in order to determine the stellar parameters. Thanks to the similar spectral wavelength range (3700 – 9000 Å) and resolution ( $R \sim 1800$ ) of the LAMOST spectra to those of the SDSS, we were able to derive the stellar parameters from the LAMOST spectra using the SSPP (see Lee et al. 2015 for detailed information). The application of the SSPP also delivered  $[Mg/Fe]$  and  $[C/Fe]$  estimates. Then, we employed the method described by Kim et al. (2022) to derive  $[N/Fe]$  from low-resolution SDSS and LAMOST spectra.

Briefly describing the method, we normalized an observed spectrum in the wavelength range of 3810 – 3900 Å, in which the CN features exist, and searched the grid of synthetic spectra for the best-fitting model with  $[N/Fe]$  by minimizing the difference between the normalized observed and synthetic spectra. In this pro-

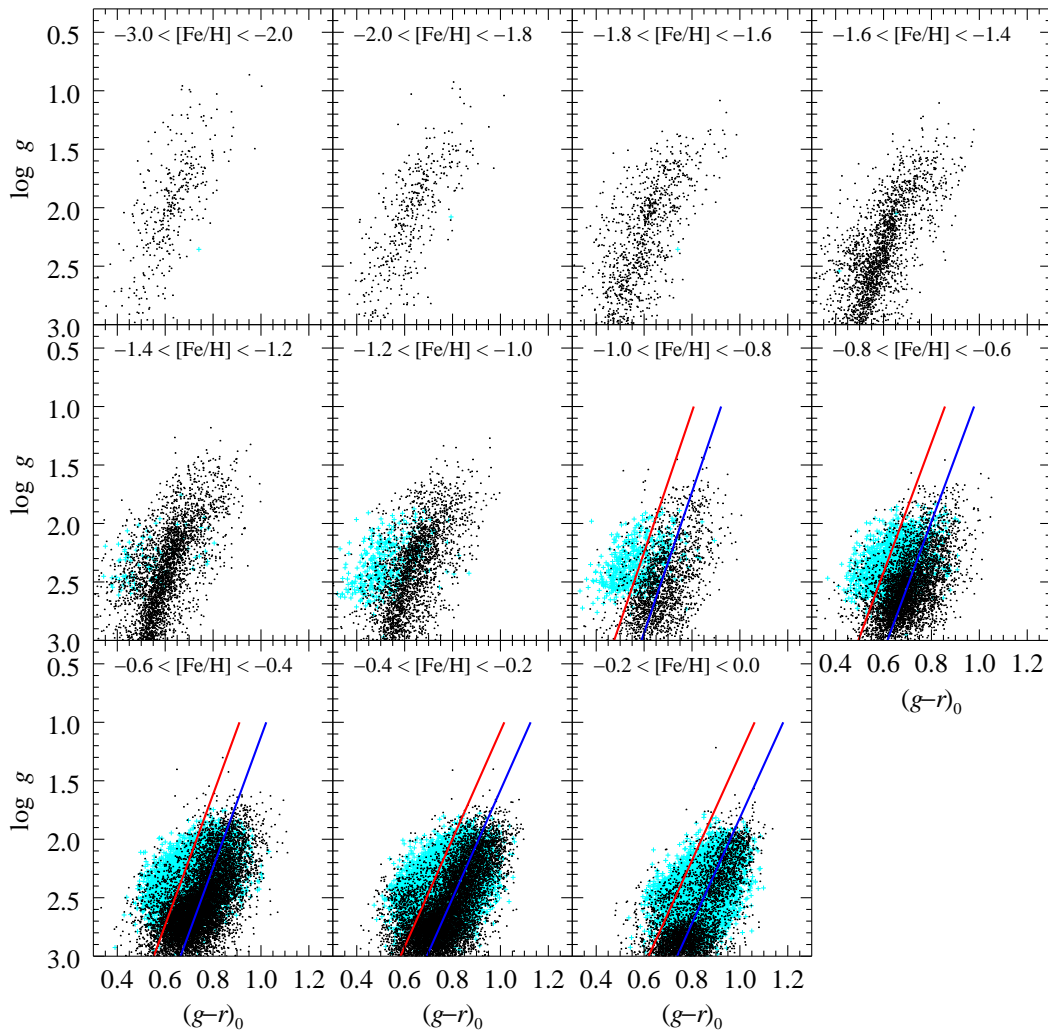


**Figure 1.** Distribution of the selected red giant-branch (RGB) stars in the  $\log g$  versus  $(g-r)_0$  plane in different metallicity intervals. The metallicity bin is indicated at the top of each panel. The red lines in the panels of the metallicity bins with  $[\text{Fe}/\text{H}] > -1.0$  are the fiducials used to remove red-clump (RC) stars. The cyan symbols are the RC stars identified by Huang et al. (2020). The fiducial line is set to  $2\sigma$  away from the main locus (blue line).

cess, we adopted  $T_{\text{eff}}$ ,  $\log g$ ,  $[\text{Fe}/\text{H}]$ , and  $[\text{C}/\text{Fe}]$  values from the SSPP and held them fixed, and varied only the  $[\text{N}/\text{Fe}]$  value to create a new trial synthetic spectrum by cubic spline interpolation over the grid of the synthetic spectra to match with the observed spectrum. The measured  $[\text{N}/\text{Fe}]$  error is typically better than 0.3 dex for signal-to-noise ratio (S/N) larger than 10 (Kim et al. 2022). The typical uncertainties of the stellar parameters ( $T_{\text{eff}}$ ,  $\log g$ , and  $[\text{Fe}/\text{H}]$ ) are about 180 K, 0.24 dex, and 0.23 dex, respectively (Lee et al. 2008a,b; Smolinski et al. 2011), while the uncertainty of measured  $[\text{C}/\text{Fe}]$  is  $\sim 0.35$  dex (Lee et al. 2013).

To select likely GC-origin stars, we first gathered giant stars by applying the following selection criteria:  $4500 \text{ K} < T_{\text{eff}} < 5500 \text{ K}$ ,  $\log g < 3.0$ ,  $-3.0 < [\text{Fe}/\text{H}] < 0.0$ ,  $13.0 < g_0 < 20.5$ , and  $\text{S}/\text{N} > 20$ . We excluded main-sequence turnoff (MSTO) stars, because they exhibit CN and CH bands that are too weak to reliably derive C and N abundance ratios, owing to their warm

temperatures. Thus, in this study we focus on red giant-branch (RGB) stars. In the selection process, we first removed the stars in the plug-plates pointing to the GCs as well as open clusters. For multiply observed stars, we chose to include the star with highest S/N. We also eliminated the stars with  $[\text{C}/\text{Fe}] > +0.15$ , because the SG stars of GCs typically possess low  $[\text{C}/\text{Fe}]$  (Martell et al. 2016; Schiavon et al. 2017a). The removal of such stars reduces the contamination from CH stars as well (Karinkuzhi & Goswami 2015).

Another source of contamination is red-clump (RC) stars, as they can be disguised as giants in our sample. We excluded RC stars by application of the following two steps. The first step is to eliminate them by cross-matching our sample of stars with the RC catalog provided by Huang et al. (2020), who compiled RC stars from LAMOST. They are indicated by cyan symbols in Figure 1, which shows our RGB stars in the  $\log g$  versus  $(g-r)_0$  plane in different metallicity

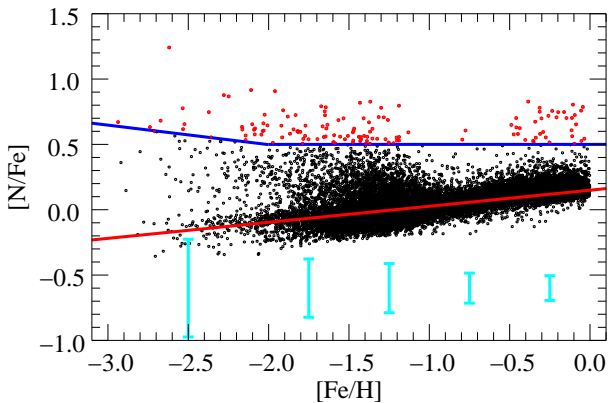


**Figure 2.** Distribution of our selected RGB stars in the  $[\text{N}/\text{Fe}]$  versus  $[\text{Fe}/\text{H}]$  space. The cyan error bars at the bottom indicate the typical uncertainties of the measured  $[\text{N}/\text{Fe}]$  over bins of 0.5 dex in  $[\text{Fe}/\text{H}]$ , except the left-most bin, which is over a 1 dex bin. The blue-solid line is the dividing line to select the N-rich stars. See the text for detailed description of deriving the line. The red dots are the N-rich population (NRP) identified in this study, while the black dots are defined as N-normal population (NNP).

ranges, as listed at the top of each panel. We can observe that most of them are located in the left side of the giant branch, proving their usefulness in removing the RC stars. In the second step, we identified the RC stars in the  $\log g$  versus  $(g-r)_0$  plane. In the panels of the metallicity region  $-1.0 < [\text{Fe}/\text{H}] < 0.0$  in Figure 1, we drew a fiducial line (red line), which is  $2\sigma$  away from the main locus (blue line) that follows the densest region. We considered stars in the left side of the fiducial line as RC stars, and removed them from the list of our RGB stars. We applied this procedure only to the stars with  $[\text{Fe}/\text{H}] > -1.0$ , because most RC stars are metal-rich ( $[\text{Fe}/\text{H}] > -1.0$ ). After these steps, we are left with a sample of about 36,800 RGB stars with available  $[\text{N}/\text{Fe}]$  estimates.

To distinguish the N-enhanced stars among the selected RGB stars, we examined their  $[\text{N}/\text{Fe}]$  distribution as a function of  $[\text{Fe}/\text{H}]$ , as shown in Figure 2. The cyan error bar indicates the typical uncertainty of the measured  $[\text{N}/\text{Fe}]$  in the interval of 0.5 dex in  $[\text{Fe}/\text{H}]$  from  $-2.0$  to  $0.0$  and 1.0 dex from  $-3.0$  to  $-2.0$ . They were derived using the stars used to calibrate the method for determining  $[\text{N}/\text{Fe}]$  in Kim et al. (2022). The typical error of the measured  $[\text{N}/\text{Fe}]$  appears to increase with decreasing  $[\text{Fe}/\text{H}]$ , and this suggests that the measured error of  $[\text{N}/\text{Fe}]$  could affect the selection of N-rich stars, especially at low metallicity. Thus, after incorporating the uncertainty of the measured  $[\text{N}/\text{Fe}]$  as a function of  $[\text{Fe}/\text{H}]$ , we carried out a simple Monte Carlo (MC) simulation to derive a selection function for the N-rich stars as follows. Assuming a Gaussian error distribution, we retrieved  $[\text{N}/\text{Fe}]$  values of individual stars using the error bar in the respective  $[\text{Fe}/\text{H}]$  bin in Figure 2. We then calculated the mean and dispersion trends of  $[\text{N}/\text{Fe}]$  as a function of  $[\text{Fe}/\text{H}]$ , and defined as N-rich population (NRP) the stars that are  $2\sigma$  or more away from the

mean  $[\text{N}/\text{Fe}]$  trend at a given  $[\text{Fe}/\text{H}]$ . We performed this MC simulation 100 times, and by taking an average of the 100 realizations we derived the mean and  $2\sigma$  trend lines as a function of  $[\text{Fe}/\text{H}]$ . However, one can guess that as the scatter of the RGB stars becomes larger with decreasing metallicity, the  $2\sigma$  placement from the mean also varies with the metallicity, that is lower  $[\text{N}/\text{Fe}]$  at higher metallicity and larger  $[\text{N}/\text{Fe}]$  at lower metallicity. Because other studies adopted the cut of  $[\text{N}/\text{Fe}] > +0.5$  to select N-rich stars (e.g., Schiavon et al. 2017a; Horta et al. 2021), we set the lower limit of the N-rich stars as  $[\text{N}/\text{Fe}] \gtrsim +0.5$  as well. As a result, the region lower than  $[\text{N}/\text{Fe}] = +0.5$  in the derived  $2\sigma$  positions was forced to set to  $[\text{N}/\text{Fe}] = +0.5$ . By doing so, we obtained the blue-solid line as a selection function in Figure 2. We conservatively took this line as a reference line to select N-rich stars in our study. The selected N-rich stars are represented by red dots in the figure, while the N-normal population (NNP) by the black dots.

We also verified from visual inspection of their spectra that the  $[\text{N}/\text{Fe}]$  estimates of the selected N-rich stars did not arise from defects in their spectra. In addition, we cross-matched our giant sample with those previously studied using the SEGUE, LAMOST, and APOGEE data (e.g., Martell et al. 2011, 2016; Schiavon et al. 2017a; Koch et al. 2019; Tang et al. 2020; Kisku et al. 2021; Fernández-Trincado et al. 2022). We found 20 stars matched with the LAMOST giant sample studied by Tang et al. (2020), and they turned out to be N-normal stars in our study. Twenty two stars were found to overlap with the SEGUE giants studied by Martell et al. (2011), and 4 objects were classified as N-rich stars in our study. We found 4 objects matched with the N-rich catalog of Fernández-Trincado et al. (2022), but unlike their estimate, our derived  $[\text{N}/\text{Fe}]$  for them is slightly lower than  $[\text{N}/\text{Fe}] \sim +0.5$ , resulting in being classified as N-normal stars in our study. The different classification among the studies is caused by the selection method employed. Tang et al. (2020) and Martell et al. (2011) used the line index of CN (at  $\sim 3850 \text{ \AA}$ ) and CH (at  $\sim 4300 \text{ \AA}$ ) features to identify N-rich stars, which may not efficiently decouple degeneracy among the line strength, temperature, and metallicity. Although Fernández-Trincado et al. (2022) selected N-rich objects based on high-resolution, near infrared spectra, we found slightly different stellar parameters for four stars, which are blamed for their N-normal status. In our study, we do not include them as N-rich stars for a self-consistent analysis. As a result, a total number of 138 N-rich stars are available for further analysis. Table 1 provides the IDs of stars that are classified as N-rich stars in our study.

### 3. SPACE VELOCITY AND ORBITAL PARAMETERS

In order to characterize the dynamical properties of our N-rich stars, we derived their space velocity components and orbital parameters. To compute the velocity components, we adopted radial velocities from the SDSS and LAMOST spectra and proper motions from Gaia Early Data Release 3 (EDR3; Gaia Collaboration et al.



2021). We did not attempt to estimate the radial velocity from the SDSS and LAMOST spectra, as each survey reduction pipeline determines the radial velocity of each star accurate to  $5 - 10 \text{ km s}^{-1}$  depending on S/N, which is the best achievable from low-resolution spectra (e.g., Yanny et al. 2009).

Distances for the SDSS stars were determined following the methodology of Beers et al. (2000, 2012), while distances for the LAMOST stars were obtained from the Value Added Catalog of LAMOST DR5 (Xiang et al. 2019). Moreover, to ensure that the two distance estimates are on the same scale, we compared the distances of SDSS and LAMOST stars with the ones determined using parallaxes from Gaia EDR3. Only stars with relative parallax errors less than 10% were retained; for these we removed the reported zero-point offset of  $-0.017 \text{ mas}$  (Lindegren et al. 2021). We obtained a difference of  $-0.031 \text{ mag}$  in the distance modulus between the SDSS stars and their Gaia parallax-based estimates, while for the LAMOST stars this offset was  $-0.001 \text{ mag}$ . We adjusted the mean differences in our sample of stars to cancel out for these systematic offsets.

For the calculation of space velocity, we adopted  $V_{\text{LSR}} = 236 \text{ km s}^{-1}$  (Kawata et al. 2019) for the rotation of the local standard of rest (LSR), a solar position of  $R_{\odot} = 8.2 \text{ kpc}$  (Bland-Hawthorn & Gerhard 2016) from the Galactic center and  $Z_{\odot} = 20.8 \text{ pc}$  (Bennett & Boby 2019) from the midplane. The adopted solar peculiar motion with respect to the LSR is taken to be  $(U, V, W)_{\odot} = (-11.10, 12.24, 7.25) \text{ km s}^{-1}$  (Schönrich et al. 2010), where the velocity components  $U$ ,  $V$ , and  $W$  are positive in the directions toward the Galactic anticenter, Galactic rotation, and North Galactic Pole, respectively. In addition, in a spherical coordinate system with an origin at the Galactic center, we derived the velocity components of  $V_r$ ,  $V_{\phi}$ , and  $V_{\theta}$ .

We also computed various orbital parameters, such as maximum ( $r_{\text{max}}$ ) and minimum ( $r_{\text{min}}$ ) distances from the Galactic center, maximum distance ( $Z_{\text{max}}$ ) from the Galactic plane, orbital eccentricity ( $e$ ) defined by  $(r_{\text{max}} - r_{\text{min}})/(r_{\text{max}} + r_{\text{min}})$ , and orbital inclination ( $i$ ) by adopting an analytic Stäckel-type potential, which has been employed by numerous studies (Chiba & Beers 2000; Carollo et al. 2007, 2010; Kim et al. 2019; Lee et al. 2019; Kim et al. 2021; Lee et al. 2023). We also derived the orbital elements of the MW’s GCs by employing their positions, proper motions, distances, and radial velocities, as provided by Vasiliev (2019).

#### 4. RESULTS AND DISCUSSION

The observed chemical peculiarity of N-enhanced stars suggests that they may have formed in environments different from those of N-normal stars. One may expect that these different environmental origins should be reflected in their metallicity distribution functions (MDFs) and dynamical properties. In this section we explore this question in detail, and consider its consequences.

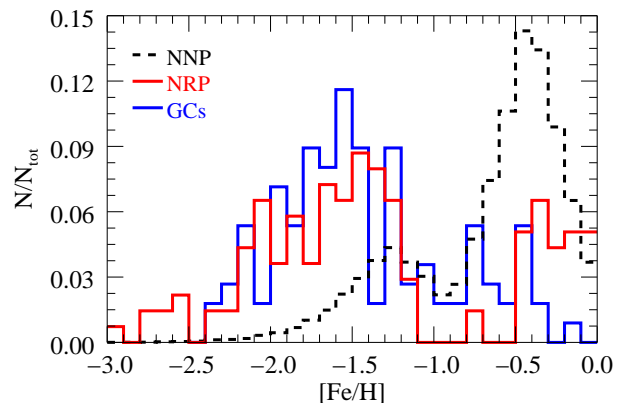


**Figure 3.** Metallicity ( $[\text{Fe}/\text{H}]$ ) distribution of NRP (red), NNP (black dashed), and MW’s GCs (blue). We did not include the GCs in the Galactic bulge. The distribution is normalized by the total number of stars in each population. The NRP is clearly more metal-poor than the NNP, and has an extended distribution. The MDF of the GCs quite well overlaps with that of the NRP in the metallicity range  $[\text{Fe}/\text{H}] < -1.0$ . The metallicity values of the GCs were adopted from the catalog by Harris (1996, 2010).

##### 4.1. Contrast in the Metallicity Distribution Between NRP and NNP

We first examined the MDFs of our NNP and NRP, as shown in Figure 3. The red histogram represents the NRP, whereas the black one applies to the NNP. We also plotted the MDF of the MW’s GCs for comparison. Note that we excluded the bulge GCs, which are identified in Massari et al. (2019), because our NRP does not include the stars near the Galactic bulge. The figure shows that the MDFs of both the NRP and NNP have two peaks, well-separated around  $[\text{Fe}/\text{H}] \sim -1.0$ , with some discrepancies between them. The NNP is represented by well-defined MDFs of the metal-rich disk and metal-poor halo populations. The disk population is dominated by the thick-disk stars and the Splash (Belokurov et al. 2020) with  $[\text{Fe}/\text{H}] > -1.0$ , while the (inner-) halo population is heavily influenced by GSE with  $[\text{Fe}/\text{H}] < -1.0$ .

The NRP has a metallicity distribution biased toward the more metal-poor and metal-rich regions; the MDF of the metal-poor stars ( $[\text{Fe}/\text{H}] < -1.0$ ) has an extended distribution down to  $[\text{Fe}/\text{H}] = -3.0$ , while the metal-rich stars ( $[\text{Fe}/\text{H}] > -1.0$ ) cut off at  $[\text{Fe}/\text{H}] \sim -0.5$ . One clear discrepancy is that the NRP is dominated by more metal-poor stars with  $[\text{Fe}/\text{H}] < -1.5$  than the NNP. This chemical dissimilarity between the NNP and NRP suggests that the NRP may have gone through a different chemical-evolution history than the NNP. A Kolmogorov-Smirnov (K-S) two-sample test indicates that the probability that the two groups of stars are drawn from a same parent population is lower than 0.1%, clear evidence for different origins.

Figure 3 also reveals that the MDF of the NRP mimics that of the MW’s GCs for  $[\text{Fe}/\text{H}] < -1.0$ . A K-S test of the MDFs in this metallicity range yields a  $p$ -value of 0.92, in other words, that the distributions

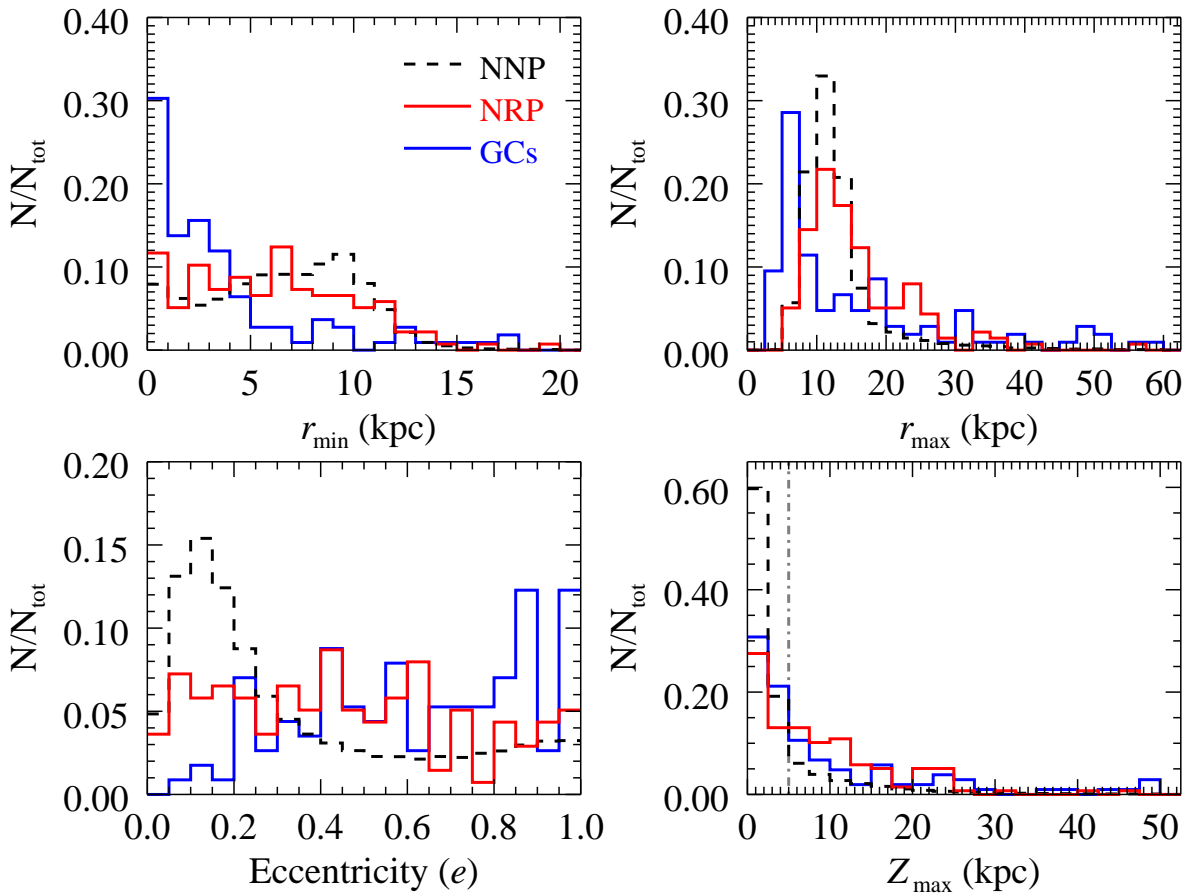


**Figure 4.** Comparisons of orbital parameters ( $r_{\min}$ ,  $r_{\max}$ ,  $e$ , and  $Z_{\max}$ ) between the NRP (red), NNP (black dashed), and GCs (blue). As in Figure 3, we excluded the bulge GCs. The distribution is normalized by the total number of stars in each group. The gray vertical line in the bottom-right panel delineates  $Z_{\max} = 5$  kpc, in which the Galactic halo system begins to dominate.

are indistinguishable, implying that a large fraction of the NRP may be escapees from existing GCs within this metallicity range. On the other hand, we obtained a  $p$ -value less than 0.001 in the same metallicity range between the GCs and NNP, a clear signature that the NNP does not come from existing GCs. The rather different shape of the MDF for  $[\text{Fe}/\text{H}] > -1.0$  between the NRP and GCs and the wide metallicity range of the NRP suggest diverse birth places for stars in the NRP.

#### 4.2. Contrast in Dynamical Characteristics Between NRP and NNP

We further searched for distinguishable properties between the NNP and NRP in their respective orbital parameter spaces, as shown in Figure 4. The typical uncertainty of each parameter is 0.6, 1.6, 1.4 kpc, and 0.04 for  $r_{\min}$ ,  $r_{\max}$ ,  $Z_{\max}$ , and  $e$ , respectively. In the figure, the NRP is represented by the red histogram, while the NNP is the black-dashed one. In each panel, we also included the distributions of the GCs for comparison. The histograms are normalized by the total number of stars in each population. A number of distinct trends are apparent. The top-left panel indicates that the  $r_{\min}$  distribution of the NNP peaks at  $r_{\min} \sim$

9 kpc, whereas that of the NRP gradually declines with increasing  $r_{\min}$ . The  $r_{\max}$  distribution for both populations peaks at  $r_{\max} \sim 11$  kpc, but there is a lingering trend of the N-enhanced stars found at larger  $r_{\max}$  than the N-normal ones. Because both the NRP and NNP have  $r_{\max} > 5.0$  kpc, no stars are bound to the Galactic bulge.

These different behaviors between the two populations are directly reflected in the eccentricity ( $e$ ) distribution shown in the bottom-left panel. The NNP is mostly populated within  $e \lesssim 0.4$ , which is associated with the disk system, while the NRP is distributed more evenly, leading to higher fraction of high- $e$  stars compared to the NNP.

In the case of  $Z_{\max}$ , as seen in the bottom-right panel, more fraction of stars in the NRP exhibit excursions that reach farther away from the Galactic plane than the NNP and the GCs. The gray-dashed line is located at  $Z_{\max} = 5$  kpc, beyond which Galactic halo stars begin to dominate. Judging from this reference line, the majority of the NRP travel through the Galactic halo region, whereas most of the NNP are confined to the Galactic disk system. Application of K-S two-sample tests for these orbital parameters yielded  $p$ -

values smaller than 0.001 for all of them, under the null hypothesis that the two groups of stars share the same parent population. These disparate dynamical properties provide further evidence for the distinct origins of the NRP and NNP.

Contrasting dynamical properties between the NRP and NNP have been reported in other studies. For example, [Tang et al. \(2020\)](#) carried out a similar kinematic analysis using about 100 metal-poor CN-strong stars from LAMOST DR5. Although their RGB sample covers a much narrower metallicity range  $-1.8 < [\text{Fe}/\text{H}] < -1.0$  than ours ( $-3.0 < [\text{Fe}/\text{H}] < 0.0$ ), they came to a similar conclusion, that their N-enhanced and N-normal stars do not share the same birthplace. Based on the finding that the orbital properties of their N-rich field stars are very similar to MW inner-halo stars, they concluded that their N-enhanced stars are likely to have originated from GCs.

We also compared the dynamical properties of the NRP with those of the GCs (blue histogram in Figure 4). Because we found very similar MDFs in the region of  $[\text{Fe}/\text{H}] < -1.0$  between the NRP and GCs in Figure 3, we carried out K-S two-sample tests in the same metallicity region for the four orbital parameters. Interestingly, we obtained  $p$ -values lower than 0.001 for  $r_{\min}$ ,  $r_{\max}$ , and  $e$ , while  $Z_{\max}$  has a  $p$ -value of 0.06. Given these low  $p$ -values, which imply different dynamical properties of their parent populations, our NRP does not appear to originate in the current MW's GCs, which contradicts the interpretation from the MDF comparison. For these disparate characteristics, one may naively think of the contribution from fully dissolved GCs, which had metallicities similar to those of the MW's GCs, resulting in the similar MDFs, but dissimilar dynamical properties. This may be partially true for the stars with  $[\text{Fe}/\text{H}] < -2.5$ , because there are no MW's GCs with  $[\text{Fe}/\text{H}] < -2.5$ . However, a more plausible explanation for the dynamical discrepancies is that some of the NRP stars in the metallicity range  $[\text{Fe}/\text{H}] < -1.0$  may be indeed escaped from GCs in the past, and they have dissimilar properties with the current GCs, because the dynamical properties of the GCs have been changed by the dynamic friction of the MW over time, while the escaped stars have not. From the comparison between NNP and GCs, we obtained the  $p$ -values of all parameters lower than 0.001, implying that the NNP is not associated with the GCs, which is consistent with the MDF comparison.

Our interpretation above partially agrees with other studies. For example, [Savino & Posti \(2019\)](#) compared the orbital properties of 57 CN-strong field stars observed in SDSS with those of the MW's GCs. They found that only 20 stars (35%) have orbital characteristics similar to the existing GCs, and recognized that the CN-strong stars with halo kinematics are expected under the GC-escapee scenario. [Carollo et al. \(2013\)](#) also reached a similar conclusion, based on the fact that both their N-enhanced field stars and the MW GCs exhibit inner-halo kinematics and orbital properties. In order to confirm which scenario is more realistic, it is neces-

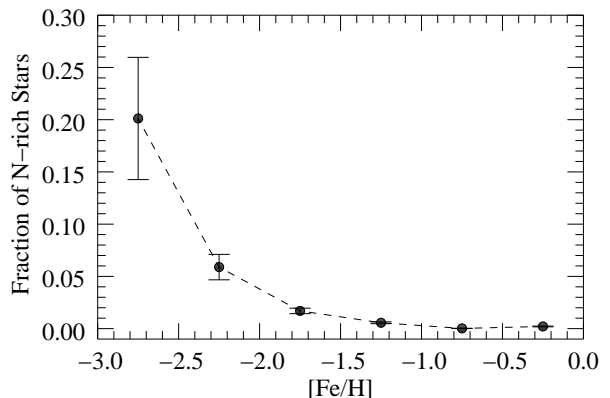


**Figure 5.** Frequency of N-rich stars as a function of  $[\text{Fe}/\text{H}]$ . The error bars are derived by bootstrap resampling.

sary to carry out a more detailed chemical-abundance analysis of the NRP stars, and compare their abundance patterns with those of the existing GCs.

### 4.3. Fractions of N-rich Stars

Given that the N-rich stars originated in GCs, the fraction of N-rich stars as a function of  $[\text{Fe}/\text{H}]$  can provide an important clue to characterizing their host systems, as well as the level of their contribution to the Galactic halo. We begin by plotting the frequency of the N-rich stars with respect to the halo field stars as a function of  $[\text{Fe}/\text{H}]$ , as shown in Figure 5. The metallicity bin size to calculate the fraction is 0.5 dex, and the error bars are based on bootstrap resampling of our programs stars. Inspection of this figure reveals that the N-rich fraction does not increase much for  $[\text{Fe}/\text{H}] > -2.0$ , while a significant rise of up to  $\sim 20\%$  occurs for  $[\text{Fe}/\text{H}] < -2.0$ , indicating a larger contribution of the GC SG stars with  $[\text{Fe}/\text{H}] < -2.0$ . The fact that there are not many GCs with  $[\text{Fe}/\text{H}] < -2.0$  (and no intact GC with  $[\text{Fe}/\text{H}] < -2.5$ ) leads us to conjecture that the fully destroyed very metal-poor (VMP;  $[\text{Fe}/\text{H}] < -2.0$ ) GCs may have in some degree contributed to the Galactic halo. As the MW's metal-poor GCs are generally older than the metal-rich counterparts ([Massari et al. 2019](#)), they have experienced more prolonged tidal interactions with the MW and were fully destroyed.

If this is the case, it may have an interesting impact on the frequency of the carbon-enhanced metal-poor (CEMP;  $[\text{Fe}/\text{H}] < -1.0$ ,  $[\text{C}/\text{Fe}] > +0.7$ ) stars in the Galactic halo. Studies show that the fraction of the CEMP stars accounts for  $\sim 10 - 20\%$  between  $[\text{Fe}/\text{H}] = -3.0$  and  $-2.0$  ([Lee et al. 2013](#); [Placco et al. 2014](#)). One can expect that, without the contribution of FG and SG stars from partially or fully dissolved GCs, which are mostly carbon-normal stars, the CEMP frequency in the metallicity range would be much higher. The observed fraction of CEMP stars has been frequently used to constrain the initial mass function (IMF) of the MW using population-synthesis models (e.g., [Komiyama et al. 2007](#); [Suda et al. 2013](#); [Lee et al. 2014](#)). The model predictions of the CEMP frequency are somewhat higher than the observed trend in that metallicity range. By

taking into account the contribution of the GC stars to the MW, the deficit in the CEMP frequency between the model and observation can be reduced, and in turn it will provide more strict constraints to the models for prediction of the IMF.

The overall NRP fraction allows us to estimate the GC contribution to the mass budget of the MW, and a number of studies have attempted to predict this over the past few years. For instance, using the metal-poor halo giants ( $-1.8 < [\text{Fe}/\text{H}] < -1.0$ ) from APOGEE DR12, [Martell et al. \(2016\)](#) attempted to calculate the fraction of N-rich stars with respect to the halo field stars, deriving a contribution of 2 – 3% of GC SG stars in the halo. Their previous work also accounted for the similar percentage ([Martell et al. 2011](#)). This has been further confirmed by [Koch et al. \(2019\)](#), who used CN strong stars from SEGUE data to compute about 2.6%. [Horta et al. \(2021\)](#) also estimated a fraction of 2.7% at 10 kpc from the Galactic center, using the APOGEE DR16 ([Jönsson et al. 2020](#)) giant sample. We derived a fraction of  $0.4 \pm 0.1\%$  of the N-rich stars in our RGB sample, which is about 6 to 7 times lower than those studies. Even if we restrict ourselves to the metallicity range  $-2.0 \leq [\text{Fe}/\text{H}] \leq -1.0$ , on which the previous studies focused, we obtained a fraction of  $0.8 \pm 0.1\%$ . The main reason for the much lower value is that our NNP sample is overwhelmed by local halo stars dominated by the GSE structure, with a MDF peak at  $[\text{Fe}/\text{H}] \sim -1.3$ , as can be appreciated in Figure 3. These stars were mostly observed in the LAMOST survey, and they are located closer to the Galactic disk than the SDSS stars. Consequently, our sample includes more N-normal disk stars than the previous studies, as can be inferred from the bottom panels of Figure 4. In this respect, considering only the SDSS giants, which reside in more distant halo region, we obtained a fraction of  $2.3 \pm 0.2\%$  for the N-rich stars, which well agrees with those of [Martell et al. \(2011\)](#) and [Koch et al. \(2019\)](#), who utilized the SEGUE spectra to derive the fractions. The different temperature range for selecting giants could be another source of the large discrepancy. The previous studies mentioned above include more cool giants ( $T_{\text{eff}} < 4500$  K), in contrast to our giant sample.

We note that the observed N-rich fractions do not directly reflect the contribution of the GC-origin stars to the Galactic halo. Depending on the assumed ratio between the FG and SG of a GC and the dissolved fraction of a GC, the total GC contribution to the halo of the MW significantly varies from study to study (17 – 50%) ([Martell & Grebel 2010](#); [Martell et al. 2011](#); [Carollo et al. 2013](#); [Koch et al. 2019](#); [Tang et al. 2020](#); [Horta et al. 2021](#)). As those parameters for GCs are not well-established at present, in this study we do not attempt to evaluate the total fraction of the GC-origin stars using the derived fraction of the N-rich stars.

Even though there are no bulge stars in our sample, it is worthwhile mentioning the situation for the NRP fraction in the Galactic bulge, as it is quite different from the Galactic halo. [Schiavon et al. \(2017a\)](#), who focused on stellar populations within  $\sim 3$  kpc of

the Galactic center, derived a fraction of 13 – 17 % of N-rich stars, which is much higher than found in the halo region. Using giants from APOGEE DR16 and a density model of the halo stellar population, [Horta et al. \(2021\)](#) estimated a fraction of 16.8% of N-rich stars with respect to N-normal stars at a distance of 1.5 kpc from the Galactic center. They further predicted, by assuming the ratio of 0.5 between the FG and SG in a GC proposed by [Schiavon et al. \(2017a\)](#) that the total contribution of disrupted GC stars to the MW accounts for 27.5% and 4.2% at 1.5 kpc and 10 kpc from the Galactic center, respectively. As discussed in [Horta et al. \(2021\)](#), the higher fraction of the N-rich stars in the inner region of the MW may be explained by more frequent merger events in the early history of the MW. During such mergers, some fraction of extragalactic-origin N-rich stars were brought into that region. In addition, the in situ formation and destruction of GCs were actively contributing, resulting in a large number of N-rich stars in the inner region of the MW. Overall, the observational data suggest that the disrupted GCs donated their stars to both the halo and bulge, with greater contributions to the bulge.

#### 4.4. Detailed Dynamical Properties of the NRP

It has been recognized for more than a decade that the Galactic GCs comprise both those that formed in situ and those that were accreted (e.g., [Forbes & Bridges 2010](#); [Massari et al. 2019](#); [Myeong et al. 2019](#); [Vasiliev 2019](#)). This means that the stars in the NRP may also originate from in situ formed GCs or accreted GCs. A detailed dynamical analysis of the NRP may be able to distinguish the progenitors of the stars in the NRP into the in situ and accreted components.

Several studies have been carried out in this regard. [Kisku et al. \(2021\)](#) found from APOGEE DR16 that, among their N-rich stars located near the Galactic bulge, the accreted stars account for about 30% of the total. They separated the accreted component using the Si abundance ratio in the  $[\text{Si}/\text{Fe}]$  versus  $[\text{Fe}/\text{H}]$  plane, and kinematically confirmed the separation as well. [Tang et al. \(2020\)](#) also cautiously reported, based on a small number of stars (4 out of 11 stars) that a substantial portion (36%) of their N-rich field stars may have been accreted by the MW. From a more extensive study, [Fernández-Trincado et al. \(2022\)](#) compiled a total of 412 unique N-rich stars that are likely to have been stripped from GCs, and they demonstrated through a kinematic analysis that they must have originated from several channels, including dissolved members of GCs brought into the MW during major-merger events such as the GSE.

Here, in order to investigate their dynamical properties and qualitatively assess the origin of their progenitors, we examine the locations of our N-rich stars in various orbital parameter spaces, as a function of  $[\text{Fe}/\text{H}]$  (left) and orbital eccentricity (right), as shown in Figure 6. The color code indicates  $[\text{Mg}/\text{Fe}]$  (left panels) and  $[\text{Fe}/\text{H}]$  (right panels) scales, and each scale is represented by the color bar at the top. In Panel (a), the



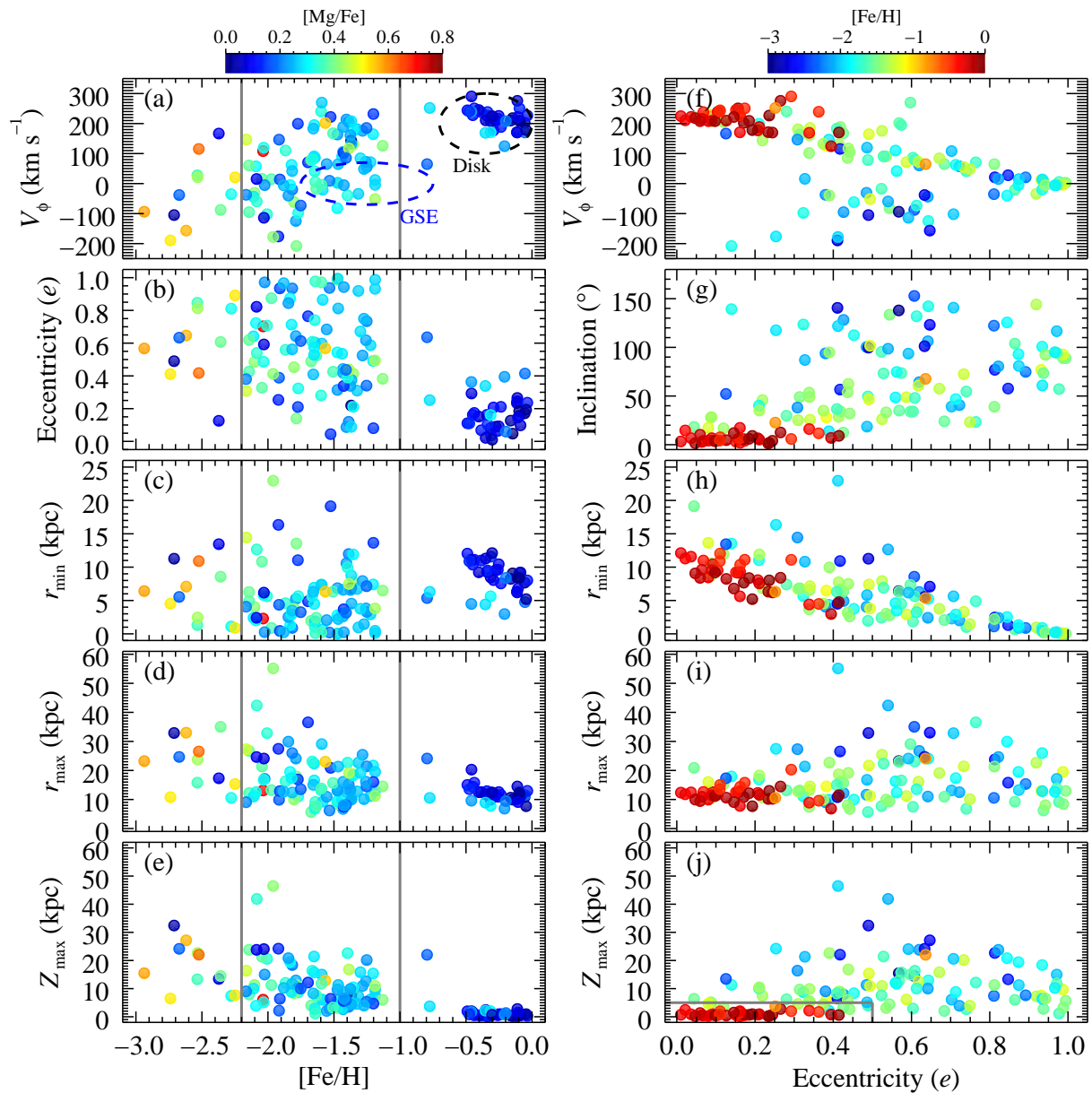


**Figure 6.** Left panels: Runs of  $V_\phi$ , eccentricity ( $e$ ),  $r_{\min}$ ,  $r_{\max}$ , and  $Z_{\max}$  with respect to  $[\text{Fe}/\text{H}]$  for stars in the NRP. The color code represents  $[\text{Mg}/\text{Fe}]$ , shown in the color bar above the column of panels. In Panel (a), the black-dashed circle represents the Galactic disk system, while the blue-dashed ellipse is the approximate region of the GSE structure based on Belokurov et al. (2018). The vertical lines denote to separate the NRP into metal-rich ( $[\text{Fe}/\text{H}] > -1.0$ ), N-rich (MRNR), metal-intermediate ( $-2.2 < [\text{Fe}/\text{H}] \leq -1.0$ ), N-rich (MINR), and metal-poor ( $[\text{Fe}/\text{H}] \leq -2.2$ ), N-rich (MPNR) stars. Right panels: Runs of  $V_\phi$ , inclination ( $i$ ),  $r_{\min}$ ,  $r_{\max}$ , and  $Z_{\max}$  with respect to eccentricity for stars in the NRP. The color code represents  $[\text{Fe}/\text{H}]$ , shown in the color bar above the column of panels. The gray box in Panel (j) indicates the division for the in situ origin adopted by Massari et al. (2019). See Section 4.4.4 for a detailed description.

black-dashed circle represents the Galactic disk system, while the blue-dashed ellipse is the approximate region of the GSE structure based on Belokurov et al. (2018).

The overall behavior of the NRP in Figure 6 is as follows. The rotation velocity  $V_\phi$  exhibits a good correlation with  $[\text{Fe}/\text{H}]$  (Panel (a)). The orbital parameters of  $r_{\max}$  and  $Z_{\max}$  show anti-correlations with  $[\text{Fe}/\text{H}]$  for  $[\text{Fe}/\text{H}] < -1.0$ . The anti-correlation becomes more prominent below  $[\text{Fe}/\text{H}] = -2.2$ , which is the peak of the MDF of the outer-halo stars (e.g., Carollo et al.

2010; Beers et al. 2012; Lee et al. 2017). We also note a well-established anti-correlation between  $r_{\min}$  and  $e$  in Panel (h). Upon close inspection of the left-column panels, we realized that it is convenient for our analysis to divide our NRP stars into at least three different groups according to the metallicity: metal-rich ( $[\text{Fe}/\text{H}] > -1.0$ ), N-rich (MRNR), metal-intermediate ( $-2.2 < [\text{Fe}/\text{H}] \leq -1.0$ ), N-rich (MINR), and metal-poor ( $[\text{Fe}/\text{H}] \leq -2.2$ ), N-rich (MPNR). The two vertical lines delineate the domains of this separation. We can confirm

that this chemical separation is qualitatively justified by well-behaved distinct dynamical properties of each metallicity group in the right-column panels, and discuss these groupings in detail below.

#### 4.4.1. Metal-poor, N-rich (MPNR) Group

The majority of the MPNR stars possess high  $[\text{Mg}/\text{Fe}]$  ( $> +0.3$ ), high eccentricity ( $e > 0.4$ ), and high inclination ( $i > 60^\circ$ ). Note that stars with  $i > 90^\circ$  have retrograde motions. We also note that most of the MPNR stars exhibit relatively low  $V_\phi$  ( $< 50 \text{ km s}^{-1}$ ) and even retrograde motion, and some of them travel farther out up to  $r_{\text{max}} \sim 35 \text{ kpc}$  and  $Z_{\text{max}} \sim 30 \text{ kpc}$  into the halo. Interestingly, a few stars even approach close to the Galactic bulge ( $r_{\text{min}} < 3 \text{ kpc}$ ). These dynamical characteristics may indicate that the host systems of some of the MPNR stars are accreted; in particular all stars with  $[\text{Fe}/\text{H}] < -2.5$  would have an ex situ origin, as no surviving MW GCs have such low metallicity. Their low  $V_\phi$  ( $< 50 \text{ km s}^{-1}$ ) also provides more evidence for an accretion origin. The hypothesis of extragalactic origin is supported by a recent study, which claimed that some of the N-rich stars in the Galactic halo are accreted from the GCs associated with Sagittarius (Sgr) dwarf galaxy (Fernández-Trincado et al. 2021a). The theoretical work by Rostami Shirazi et al. (2022) also upholds this idea. These authors simulated the escaped fraction of GCs in a dwarf galaxy, and argued that many dwarf galaxies, such as Sgr, Fornax, Sculptor, etc. in the MW have lost some of their GCs while interacting with the MW.

One may think that the stars with moderate rotation velocity ( $V_\phi > 50 \text{ km s}^{-1}$ ) and  $[\text{Fe}/\text{H}] > -2.5$  originate from partially or fully disrupted GCs, which formed in situ because the MW's GCs exhibit an average rotation velocity of  $V_\phi = 50 - 80 \text{ km s}^{-1}$  (Vasiliev 2019).

#### 4.4.2. Metal-intermediate, N-rich (MINR) Group

The MINR stars have a wide range of  $V_\phi$ ,  $e$ ,  $r_{\text{min}}$ , and  $i$ , while their  $r_{\text{max}}$  and  $Z_{\text{max}}$  values are concentrated in a relatively narrow range. These features imply diverse origins at similar metallicities.

According to Vasiliev (2019), the GCs within 10 kpc from the Galactic center have a mean azimuthal velocity in the range  $50 - 80 \text{ km s}^{-1}$ , while the ones in the outer region exhibit strongly radial orbits. In addition, the GCs that reside in the inner halo are relatively more metal-rich ( $[\text{Fe}/\text{H}] > -2.0$ ). These aspects suggest that a large fraction of our MINR stars with moderate rotation velocity ( $V_\phi > 50 \text{ km s}^{-1}$ ) and low  $e$  ( $< 0.4$ ) may have been stripped from existing GCs, which is in accordance with the interpretation from the MDF comparison in Section 4.1.

Among our MINR stars, the ones in the blue ellipse in Panel (a) with high eccentricity ( $e > 0.7$ ) and  $V_\phi \sim 0.0 \text{ km s}^{-1}$  may have originated from disrupted GCs that belonged to the GSE during its merger with the MW, as their dynamical properties coincide with those of the GSE. Indeed, Myeong et al. (2018) reported

about 8 GCs associated with the GSE, with  $e > 0.8$  and  $V_\phi < 50 \text{ km s}^{-1}$ . We observe that a small fraction of our MINR stars have orbits that pass close to the Galactic center ( $r_{\text{min}} < 3 \text{ kpc}$ , see Panel (h)), but are not bound to the bulge, because of their  $r_{\text{max}} > 5 \text{ kpc}$ . Since these stars have strong radially biased orbits and  $e > 0.8$ , their host GCs are highly likely to originate from the GSE merger event, as claimed by Myeong et al. (2018). The fact that the GSE stars with  $[\text{Fe}/\text{H}] < -1.0$  on average exhibit  $[\text{Mg}/\text{Fe}] > +0.1$  (e.g., Lee et al. 2023) reinforces the above claim. Note that, of the likely members of the GC SG, the stars with relatively low Mg abundance ratios ( $[\text{Mg}/\text{Fe}] < 0.0$ ) are regarded as an extragalactic origin, because the low Mg abundance ratio along with high Al is reported in some GCs in M31 and the Large Magellanic Cloud (Colucci et al. 2009, 2012; Fernández-Trincado et al. 2020b). Other studies also reported low- $[\text{Mg}/\text{Fe}]$  stars among the candidates for dissolved GC members (Fernández-Trincado et al. 2016, 2017, 2019). Thus, we expect that at least a few stars with  $[\text{Mg}/\text{Fe}] \sim 0.0$  among our MINR stars may fall in that category.

We also note a handful of stars with orbital eccentricities  $e = 0.4 - 0.6$  and chemical abundances of  $[\text{Fe}/\text{H}] \sim -1.3$  and  $[\text{Mg}/\text{Fe}] \sim +0.2$ , which are characteristic of the Sgr dwarf galaxy (Fernández-Trincado et al. 2021a). As Fernández-Trincado et al. (2021a) reported possible member stars of M54, these stars are likely to have come from disrupted GCs of the Sgr dwarf galaxy. Furthermore, because a small portion of the MINR stars share metallicity ( $[\text{Fe}/\text{H}] < -1.7$ ) and dynamical properties ( $V_\phi < -50 \text{ km s}^{-1}$  and  $e = 0.5 - 0.6$ ) with those of the Sequoia event (Myeong et al. 2019; Naidu et al. 2020), we cannot rule out their association with the Sequoia dwarf galaxy. Through a kinematic analysis of MW's GCs, Massari et al. (2019) also claimed that about 5% of the MW's GCs have originated from the Sequoia event.

#### 4.4.3. Metal-rich, N-rich (MRNR) Group

The MRNR population ( $[\text{Fe}/\text{H}] > -1.0$ ) has mostly low eccentricity ( $e \lesssim 0.3$ ) and low inclination ( $i \lesssim 20^\circ$ ) with high prograde motions ( $V_\phi \gtrsim 160 \text{ km s}^{-1}$ ) and low  $Z_{\text{max}}$  ( $\lesssim 3 \text{ kpc}$ ), indicating that they are confined close to the Galactic plane. We also observe that most of the MRNR stars are located in the rotationally supported inner-disk region ( $r_{\text{min}} < 12 \text{ kpc}$ ), and do not travel far away ( $r_{\text{max}} < 16 \text{ kpc}$ ) from the Galactic center. Their Mg abundance ratio is low ( $[\text{Mg}/\text{Fe}] < 0.2$ ), as in disk stars. Because our MRNR stars do not follow the MDF of the existing GCs (see Figure 3), and their MDF is shifted to the more metal-rich region, they are not likely to be connected with the existing GCs. Rather, these dynamical and chemical features suggest that most of the MRNR stars may have originated from fully destroyed metal-rich GCs formed in situ in the disk, as envisaged by Fernández-Trincado et al. (2021b).

However, there are a few stars with intriguing distinct kinematics and somewhat high  $[\text{Mg}/\text{Fe}] \gtrsim +0.2$ , which diverge from the typical trend. Among them, one star draws our attention. Its eccentricity and metallic-

ity are  $e \sim 0.6$  and  $[\text{Fe}/\text{H}] \sim -0.8$ . This star may be associated with the progenitor of the GSE merger event, because it is located near the GSE structure in Panel (a) of Figure 6. It is also plausible that it originates from the GSE-induced starburst, as recently reported by a few studies (Myeong et al. 2022; An et al. 2023; Lee et al. 2023). The other star, at  $[\text{Fe}/\text{H}] \sim -0.8$  and  $V_\phi \sim 240 \text{ km s}^{-1}$ , may be in this category as well. However, it cannot be ruled out that, because its metallicity and eccentricity are overlapped with the Splash stars, it could be a dynamically heated star from the GSE merger after its host GC formed in situ and was disrupted in the disk. Its relatively high  $[\text{Mg}/\text{Fe}]$  value ( $[\text{Mg}/\text{Fe}] \sim +0.2$ ) supports this scenario. It is known that the GSE stars exhibit low  $[\text{Mg}/\text{Fe}]$  ( $< +0.1$ ) at  $[\text{Fe}/\text{H}] > -1.0$ , while the Splash shows high  $[\text{Mg}/\text{Fe}]$  ( $> +0.2$ ) for  $[\text{Fe}/\text{H}] > -1.0$  (Belokurov et al. 2020; Lee et al. 2023). A more detailed chemical-abundance pattern is required to unveil this star's origin.

#### 4.4.4. In Situ Versus Accretion

Taking into account our qualitative assessment of the possible origins of our NRP stars from the dynamical characterization, it is clear that most of our NRP stemmed from diverse groups of in situ formed GCs and ex situ formed GCs. There may not be clear cuts to separate the accreted origin from our NRP sample. Nonetheless, based on the chemical and dynamical properties of the NRP, at least we can follow the procedure devised by Massari et al. (2019) to identify the stars with the accretion origin. They carried out a kinematic analysis of MW's GCs with their ages, and divided them to in situ and accreted populations. They found that 40% of the GCs likely formed in situ, and 35% are possibly associated with GSE, the Sgr dwarf galaxy, the progenitor of the Helmi streams, and the Sequoia galaxy. The rest are likely to have heterogeneous origins.

By simply adopting their approach, we can divide our NRP stars into in situ and accreted components, as shown in Panel (j) of Figure 6. Note that in the panel, instead of the circularity that Massari et al. (2019) used, we employed the eccentricity. Both parameters are good indicators for the orbital paths of a star. We regarded the N-rich stars with  $Z_{\text{max}} < 5 \text{ kpc}$ ,  $e < 0.5$ , and  $V_\phi > 0 \text{ km s}^{-1}$  as the in situ population. We adopted  $e < 0.5$ , since the disk stars can have the eccentricity as high as  $e \sim 0.5$  (Lee et al. 2011b; Han et al. 2020). These stars mostly correspond to the ones inside the gray box in the panel. From this exercise, we obtained a fraction of  $33.5 \pm 4.7\%$  for the in situ component, which is not far from that of Massari et al. (2019). We note, however, that by comparing with the E-MOSAICS simulations of MW-mass galaxies and their GC populations (Pfeffer et al. 2018; Kruijssen et al. 2019a), Kruijssen et al. (2019b) predicted that 67 (43%) out of 157 MW's GCs in the Harris (1996, 2010) catalog were accreted, resulting in a fraction of 57% for the in situ origin, which is higher than ours and that of Massari et al. (2019).

In addition to the above exercise, we have carried

out simple calculations to estimate the fraction of the stars with accretion origin in each metallicity group by distinguishing them from those with an in situ origin. For this to work, we introduced three criteria for the in situ origin:  $V_\phi > 50 \text{ km s}^{-1}$ ,  $Z_{\text{max}} < 5 \text{ kpc}$ , and  $e < 0.7$ . The rotation velocity cut comes from the fact that the overall rotation velocity of the GCs within 10 kpc from the Galactic center is larger than  $50 \text{ km s}^{-1}$  (Vasiliev 2019). It is also taken into account that the GSE stars have on average  $V_\phi = 0 \text{ km s}^{-1}$ , with a  $V_\phi$  dispersion of  $\sim 50 \text{ km s}^{-1}$  (Belokurov et al. 2020). The  $Z_{\text{max}}$  condition is adopted from Massari et al. (2019). The last criterion is reflected by eliminating the GSE-origin stars, as most of them have high  $e$  ( $> 0.7$ ). We imposed the  $e$  cut to only the MINR group, because it has many stars with GSE kinematics. We regarded the stars that do not simultaneously satisfy these cuts as having an ex situ origin.

By applying the above cuts to the MPNR, MINR, and MRNR groups, we obtained an accreted fraction of  $98 \pm 2\%$  for the MPNR group,  $86 \pm 4\%$  for the MINR group, and  $3 \pm 3\%$  for the MRNR group; the total fraction of stars with ex situ origins among our NRP is  $64 \pm 4\%$ . The fraction and its associated error were the mean and standard deviation derived by a Monte Carlo simulation of resampling each group of stars 10,000 times. When resampling, the uncertainty of each parameter was incorporated. Of course, all of the stars in these fractions may not have an ex situ origin, as pointed out by Massari et al. (2019), and our derived fraction may only suggest that a substantial number of the N-rich stars may have the ex situ origin.

Our derived fraction (64%) of the NRP stars with an ex situ origin is much higher than 43% reported by Kruijssen et al. (2019b). This is mainly due to how we define the ex situ origin, especially using the dynamical properties. As Kruijssen et al. (2019a) demonstrated from their simulations of the E-MOSAICS galaxies, about half of the GCs with  $[\text{Fe}/\text{H}] < -1.5$  are predicted to have formed in situ in the early assembly history of the MW. Providing that these metal-poor GCs do not exhibit disk-like kinematics at present, which is highly likely because they may have experienced continuous perturbations by the MW over a protracted period, they tend to be assigned an ex situ origin, resulting in a higher fraction of the ex situ NRP stars. Considering this, and the fact that the current GCs of the MW are mostly located within  $Z_{\text{max}} = 10 \text{ kpc}$ , as can be seen in the bottom-right panel of Figure 4, if we relax the condition for the in situ origin to have  $Z_{\text{max}} < 10 \text{ kpc}$ , we obtain a slightly lower fraction of 53% for the ex situ origins. Interestingly, using the Na-abundance ratios measured from the SDSS low-resolution spectra, Koo et al. (2022) derived a fraction of 67.8% for the accreted origin among the Na-enhanced stars, which are believed to originate from GCs, in excellent agreement with our estimate ( $64 \pm 4\%$ ) within the error.

To sum up, the existence of dynamical distinctions in each chemical group among our NRP stars indicates that the stars within each group do not share a sin-



gle common origin. A simple method for distinguishing the in situ origin reveals that, although about 34% of our NRP stars seem to share an origin with the in situ formed GCs, the origins for the rest are not associated with those of typical Galactic populations, but are of extragalactic origin, likely to be associated with the GSE, Sgr dwarf galaxy, and Sequoia. However, as we have emphasized, the fraction of accreted origin stars strongly depends on how they are defined.

## 5. SUMMARY AND CONCLUSIONS

We have identified 138 N-rich stars from low-resolution SDSS and LAMOST spectra, covering the metallicity range of  $-3.0 < [\text{Fe}/\text{H}] < 0.0$ , and compared their chemical and dynamical properties with those of the N-normal stars. The MDF of the NRP is well-matched by the canonical metal-rich disk and metal-poor halo populations, whereas the NRP has a more extended distribution toward the metal-rich and metal-poor regime. The MDF of the NRP looks very similar to that of the MW's GCs in the range of  $[\text{Fe}/\text{H}] < -1.0$ , but, K-S tests for the orbital parameters yielded  $p$ -values of less than 0.001 in the same metallicity range. These results may suggest that the escaped stars from the existing GCs account for a very small fraction among our N-rich stars. Or more plausibly, this can be explained by orbit alteration of the present GCs by dynamical friction of the MW, resulting in the different dynamical properties between our NRP (GC-escaped stars) and the GCs.

We observe a significant rise up to  $\sim 20\%$ , of the fraction of the N-rich stars below  $[\text{Fe}/\text{H}] = -2.0$ , and infer that fully destroyed VMP GCs ( $[\text{Fe}/\text{H}] < -2.0$ ) may have contributed in some degree to the Galactic halo, because there are not many surviving GCs with  $[\text{Fe}/\text{H}] < -2.0$ . The overall fraction of the NRP in our giant sample is  $0.4 \pm 0.1\%$ , which is much lower than previous studies (2 – 3%), which we believe is due to the larger fraction of GSE stars and disk stars in our sample, compared to previous studies.

The overall dynamical properties between the NRP and NNP are dissimilar, indicating that the N-rich stars arose from diverse origins. We conduct more detailed dynamical analysis of the N-rich stars, dividing them into three groups according to the metallicity: the MPNR, MINR, and MRNR groups. We find that, not only does each metallicity group exhibit distinct dynamical properties, but the N-enhanced stars within each group show different characteristics in their dynamical parameters. Guided by the orbital properties of the MW GCs that are believed to be formed in situ, we attempt to estimate the fraction of the accreted origin in each group. We obtain an accreted fraction of  $98 \pm 2\%$ ,  $86 \pm 4\%$ , and  $3 \pm 3\%$  for the MPNR, MINR, and MRNR groups, respectively. These estimates suggest that almost all of the MPNR stars come from fully/partially disrupted accreted metal-poor GCs, whereas nearly all of the MRNR stars arise from fully disrupted GCs that formed in situ in the Galactic disk system. The MINR group is dominated by the accreted stars associated with the GSE, Sgr dwarf

galaxy, and Sequoia, but still a small fraction of them may originate from the existing GCs. Although overall, the ex situ origins in our NRP accounts for  $64 \pm 4\%$ , according to the selection process of the in situ origin stars, the fraction is expected to be revised based on future analyses of much larger samples.

To conclude, the NRP stars do not share a single common origin. A substantial fraction of the N-rich stars appear to originate from in situ formed GCs. However, more than 60% of NRP stars do not appear to be associated with stars of typical Galactic populations, suggesting they have extragalactic origins such as GSE, Sgr dwarf galaxies, and Sequoia, as well as from other presently unrecognized progenitors. In this study, we attempted to present the possible origin of distinct stellar population in each group, based on the dynamical parameters and chemistry ( $[\text{Fe}/\text{H}]$  and  $[\text{Mg}/\text{Fe}]$ ). However, because the dynamical and chemical properties of the stars in each group are somewhat overlapped with each other and the chemical information is limited to clearly decompose the distinct stellar populations, more detailed chemical-abundance analysis of the stars in each group is absolutely required, and their abundance patterns of several elements should be compared with those of the existing GCs and stars of other dwarf galaxies to disentangle their diverse origin. In line with this, we plan to carry out high-resolution spectroscopic follow-up observations for some of our N-rich stars.

## ACKNOWLEDGMENTS

We thank an anonymous referee for a careful review of this paper, which has improved the clarity of its presentation. Y.S.L. acknowledges support from the National Research Foundation (NRF) of Korea grant funded by the Ministry of Science and ICT (NRF-2021R1A2C1008679). Y.S.L. also gratefully acknowledges partial support for his visit to the University of Notre Dame from OISE-1927130: The International Research Network for Nuclear Astrophysics (IReNA), awarded by the US National Science Foundation. Y.K.K. acknowledges support from Basic Science Research Program through the NRF of Korea funded by the Ministry of Education (NRF-2021R1A6A3A01086446). T.C.B. acknowledges partial support for this work from grant PHY 14-30152; Physics Frontier Center/JINA Center for the Evolution of the Elements (JINA-CEE), awarded by the U.S. National Science Foundation.

Funding for the Sloan Digital Sky Survey IV has been provided by the Alfred P. Sloan Foundation, the U.S. Department of Energy Office of Science, and the Participating Institutions.

SDSS-IV acknowledges support and resources from the Center for High Performance Computing at the University of Utah. The SDSS website is [www.sdss.org](http://www.sdss.org).

SDSS-IV is managed by the Astrophysical Research Consortium for the Participating Institutions of the SDSS Collaboration including the Brazilian Participation Group, the Carnegie Institution for Science, Carnegie Mellon University, Center for Astrophysics



— Harvard & Smithsonian, the Chilean Participation Group, the French Participation Group, Instituto de Astrofísica de Canarias, The Johns Hopkins University, Kavli Institute for the Physics and Mathematics of the Universe (IPMU) / University of Tokyo, the Korean Participation Group, Lawrence Berkeley National Laboratory, Leibniz Institut für Astrophysik Potsdam (AIP), Max-Planck-Institut für Astronomie (MPIA Heidelberg), Max-Planck-Institut für Astrophysik (MPA Garching), Max-Planck-Institut für Extraterrestrische Physik (MPE), National Astronomical Observatories of China, New Mexico State University, New York University, University of Notre Dame, Observatório Nacional / MCTI, The Ohio State University, Pennsylvania State University, Shanghai Astronomical Observatory, United Kingdom Participation Group, Universidad Nacional Autónoma de México, University of Arizona, University of Colorado Boulder, University of Oxford, University of Portsmouth, University of Utah, University of Virginia, University of Washington, University of Wisconsin, Vanderbilt University, and Yale University.

The Guoshoujing Telescope (the Large Sky Area Multi- Object Fiber Spectroscopic Telescope, LAMOST) is a National Major Scientific Project which is built by the Chinese Academy of Sciences, funded by the National Development and Reform Commission, and operated and managed by the National Astronomical Observatories, Chinese Academy of Sciences.

## REFERENCES

- Abdurro’uf, Accetta, K., Aerts, C., et al. 2022, The Seventeenth Data Release of the Sloan Digital Sky Surveys: Complete Release of MaNGA, MaStar, and APOGEE-2 Data, *ApJS*, 259, 35
- Allende Prieto, C., Sivarani, T., Beers, T. C., et al. 2008, The SEGUE Stellar Parameter Pipeline. III. Comparison with High-Resolution Spectroscopy of SDSS/SEGUE Field Stars, *AJ*, 136, 2070
- An, D., Beers, T. C., Lee, Y. S., & Masseron, T. 2023, A Blueprint for the Milky Way’s Stellar Populations. IV. Spectrum-based Empirical Corrections and the Galactic Starburst Sequence, *ApJ*, submitted, [arXiv:2210.07542](https://arxiv.org/abs/2210.07542)
- Bastian, N., & Lardo, C. 2018, Multiple Stellar Populations in Globular Clusters, *ARA&A*, 56, 83
- Baumgardt, H., & Vasiliev, E. 2021, Accurate distances to Galactic globular clusters through a combination of Gaia EDR3, HST, and literature data, *MNRAS*, 505, 5957
- Beers, T. C., Chiba, M., Yoshii, Y., et al. 2000, Kinematics of Metal-poor Stars in the Galaxy. II. Proper Motions for a Large Nonkinematically Selected Sample, *AJ*, 119, 2866
- Beers, T. C., Carollo, D., Ivezić, Ž., et al. 2012, The Case for the Dual Halo of the Milky Way, *ApJ*, 746, 34
- Belokurov, V., Erkal, D., Evans, N. W., Koposov, S. E., & Deason, A. J. 2018, Co-formation of the disc and the stellar halo, *MNRAS*, 478, 611
- Belokurov, V., Sanders, J. L., Fattahi, A., et al. 2020, The biggest splash, *MNRAS*, 494, 3880
- Bennett, M., & Bovy, J. 2019, Vertical waves in the solar neighbourhood in Gaia DR2, *MNRAS*, 482, 1417
- Bland-Hawthorn, J., & Gerhard, O. 2016, The Galaxy in Context: Structural, Kinematic, and Integrated Properties, *ARA&A*, 54, 529
- Carollo, D., Beers, T. C., Lee, Y. S., et al. 2007, Two stellar components in the halo of the Milky Way, *NATURE*, 450, 1020
- Carollo, D., Beers, T. C., Chiba, M., et al. 2010, Structure and Kinematics of the Stellar Halos and Thick Disks of the Milky Way Based on Calibration Stars from Sloan Digital Sky Survey DR7, *ApJ*, 712, 692
- Carollo, D., Martell, S. L., Beers, T. C., & Freeman, K. C. 2013, CN Anomalies in the Halo System and the Origin of Globular Clusters in the Milky Way, *ApJ*, 769, 87
- Carretta, E., Bragaglia, A., Gratton, R. G., et al. 2009, Na-O anticorrelation and HB. VII. The chemical composition of first and second-generation stars in 15 globular clusters from GIRAFFE spectra, *A&A*, 505, 117
- Carretta, E., Bragaglia, A., Gratton, R. G., et al. 2010, Properties of stellar generations in globular clusters and relations with global parameters, *A&A*, 516, A55
- Carretta, E. 2016, Globular clusters and their contribution to the formation of the Galactic halo, *The General Assembly of Galaxy Halos: Structure, Origin and Evolution*, 317, 97
- Chiba, M., & Beers, T. C. 2000, Kinematics of Metal-poor Stars in the Galaxy. III. Formation of the Stellar Halo and Thick Disk as Revealed from a Large Sample of Nonkinematically Selected Stars, *AJ*, 119, 2843
- Colucci, J. E., Bernstein, R. A., Cameron, S., McWilliam, A., & Cohen, J. G. 2009, M31 Globular Cluster Abundances from High-Resolution, Integrated-Light Spectroscopy, *ApJ*, 704, 385
- Colucci, J. E., Bernstein, R. A., Cameron, S. A., & McWilliam, A. 2012, Globular Cluster Abundances from High-resolution, Integrated-light Spectroscopy. IV. The Large Magellanic Cloud:  $\alpha$ , Fe-peak, Light, and Heavy Elements, *ApJ*, 746, 29
- Cui, X.-Q., Zhao, Y.-H., Chu, Y.-Q., et al. 2012, The Large Sky Area Multi-Object Fiber Spectroscopic Telescope (LAMOST), *RAA*, 12, 1197
- Elmegreen, B. G., & Hunter, D. A. 2010, On the Disruption of Star Clusters in a Hierarchical Interstellar Medium, *ApJ*, 712, 604
- Fernández-Trincado, J. G., Robin, A. C., Moreno, E., et al. 2016, Discovery of a Metal-poor Field Giant with a Globular Cluster Second-generation Abundance Pattern, *ApJ*, 833, 132
- Fernández-Trincado, J. G., Zamora, O., Garcá-Hernández, D. A., et al. 2017, Atypical Mg-poor Milky Way Field Stars with Globular Cluster Second-generation-like Chemical Patterns, *ApJL*, 846, L2
- Fernández-Trincado, J. G., Beers, T. C., Tang, B., et al. 2019, Chemodynamics of newly identified giants with a globular cluster like abundance patterns in the bulge, disc, and halo of the Milky Way, *MNRAS*, 488, 2864
- Fernández-Trincado, J. G., Beers, T. C., Minniti, D., et al. 2020b, Discovery of a Large Population of Nitrogen-Enhanced Stars in the Magellanic Clouds, *ApJ*, 903, L17
- Fernández-Trincado, J. G., Beers, T. C., Minniti, D., et al. 2021a, APOGEE spectroscopic evidence for chemical anomalies in dwarf galaxies: The case of M 54 and Sagittarius, *A&A*, 648, A70
- Fernández-Trincado, J. G., Beers, T. C., Queiroz, A. B. A., et al. 2021b, APOGEE-2 Discovery of a Large Population of Relatively High-Metallicity Globular Cluster Debris, *ApJ*, 918, L37
- Fernández-Trincado, J. G., Beers, T. C., Barbuy, B., et al. 2022, Galactic ArchaeoLogIcaL ExcavatiOns

- (GALILEO). I. An updated census of APOGEE N-rich giants across the Milky Way, *A&A*, 663, A126
- Forbes, D. A., & Bridges, T. 2010, Accreted versus in situ Milky Way globular clusters, *MNRAS*, 404, 1203
- Gaia Collaboration, Brown, A. G. A., Vallenari, A., et al. 2021, Gaia Early Data Release 3. Summary of the contents and survey properties, *A&A*, 649, A1
- Gratton, R., Sneden, C., & Carretta, E. 2004, Abundance Variations Within Globular Clusters, *ARA&A*, 42, 385
- Han, D. R., Lee, Y. S., Kim, Y. K., & Beers, T. C. 2020, Insights into the Formation and Evolution History of the Galactic Disk System, *ApJ*, 896, 14
- Hanke, M., Koch, A., Prudil, Z., Grebel, E. K., & Bastian, U. 2020, Purveyors of fine halos. II. Chemodynamical association of halo stars with Milky Way globular clusters, *A&A*, 637, A98
- Hasselquist, S., Shetrone, M., Cunha, K., et al. 2016, Identification of Neodymium in the Apogee H-Band Spectra, *ApJ*, 833, 81
- Harris, W. E. 1996, A Catalog of Parameters for Globular Clusters in the Milky Way, *AJ*, 112, 1487
- Harris, W. E. 2010, A New Catalog of Globular Clusters in the Milky Way, [arXiv:1012.3224](https://arxiv.org/abs/1012.3224)
- Helmi, A., Babusiaux, C., Koppelman, H. H., et al. 2018, The merger that led to the formation of the Milky Way's inner stellar halo and thick disk, *NATURE*, 563, 85
- Horta, D., Mackereth, J. T., Schiavon, R. P., et al. 2021, The contribution of N-rich stars to the Galactic stellar halo using APOGEE red giants, *MNRAS*, 500, 5462
- Huang, Y., Schönrich, R., Zhang, H., et al. 2020, Mapping the Galactic Disk with the LAMOST and Gaia Red Clump Sample. I. Precise Distances, Masses, Ages, and 3D Velocities of 140,000 Red Clump Stars, *ApJS*, 249, 29
- Hughes, M. E., Pfeffer, J. L., Martig, M., et al. 2020, The  $[\alpha/\text{Fe}]$ - $[\text{Fe}/\text{H}]$  relation in the E-MOSAICS simulations: its connection to the birth place of globular clusters and the fraction of globular cluster field stars in the bulge, *MNRAS*, 491, 4012
- Jönsson, H., Holtzman, J. A., Allende Prieto, C., et al. 2020, APOGEE Data and Spectral Analysis from SDSS Data Release 16: Seven Years of Observations Including First Results from APOGEE-South, *AJ*, 160, 120
- Karinkuzhi, D., & Goswami, A. 2015, Chemical analysis of CH stars - II. Atmospheric parameters and elemental abundances, *MNRAS*, 446, 2348
- Kawata, D., Bovy, J., Matsunaga, N., & Baba, J. 2019, Galactic rotation from Cepheids with Gaia DR2 and effects of non-axisymmetry, *MNRAS*, 482, 40
- Kim, C., Lee, Y. S., Beers, T. C., & Masseron, T. 2022, Estimation of Nitrogen-to-Iron Abundance Ratios from Low-Resolution Spectra, *JKAS*, 55, 23
- Kim, Y. K., Lee, Y. S., & Beers, T. C. 2019, Dependence of Galactic Halo Kinematics on the Adopted Galactic Potential, *ApJ*, 882, 176
- Kim, Y. K., Lee, Y. S., Beers, T. C., et al. 2021, Evidence for Multiple Accretion Events in the Gaia-Sausage/Enceladus Structures, *ApJL*, 911, L21
- Kisku, S., Schiavon, R. P., Horta, D., et al. 2021, An enquiry on the origins of N-rich stars in the inner Galaxy based on APOGEE chemical compositions, *MNRAS*, 504, 1657
- Koch, A., Grebel, E. K., & Martell, S. L. 2019, Purveyors of fine halos: Re-assessing globular cluster contributions to the Milky Way halo buildup with SDSS-IV, *A&A*, 625, A75
- Komiya, Y., Suda, T., Minaguchi, H., et al. 2007, The Origin of Carbon Enhancement and the Initial Mass Function of Extremely Metal-poor Stars in the Galactic Halo, *ApJ*, 658, 367
- Koo, J.-R., Lee, Y. S., Park, H.-J., Kim, Y. K., & Beers, T. C. 2022, Determination of Sodium Abundance Ratio from Low-resolution Stellar Spectra and Its Applications, *ApJ*, 925, 35
- Kruijssen, J. M. D., Pelupessy, F. I., Lamers, H. J. G. L. M., et al. 2011, Modelling the formation and evolution of star cluster populations in galaxy simulations, *MNRAS*, 414, 1339
- Kruijssen, J. M. D., Pelupessy, F. I., Lamers, H. J. G. L. M., et al. 2012, Formation versus destruction: the evolution of the star cluster population in galaxy mergers, *MNRAS*, 421, 1927
- Kruijssen, J. M. D., Pfeffer, J. L., Crain, R. A., & Bastian, N. 2019a, *MNRAS*, The E-MOSAICS project: tracing galaxy formation and assembly with the age-metallicity distribution of globular clusters, 486, 3134
- Kruijssen, J. M. D., Pfeffer, J. L., Reina-Campos, M., et al. 2019b, *MNRAS*, The formation and assembly history of the Milky Way revealed by its globular cluster population, 486, 3180
- Lee, A., Lee, Y. S., Kim, Y. K., et al. 2023, Chemodynamical Analysis of Metal-rich High-eccentricity Stars in the Milky Way's Disk, *ApJ*, 945, 56
- Lee, Y. S., Beers, T. C., Sivarani, T., et al. 2008a, The SEGUE Stellar Parameter Pipeline. I. Description and Comparison of Individual Methods, *AJ*, 136, 2022
- Lee, Y. S., Beers, T. C., Sivarani, T., et al. 2008b, The SEGUE Stellar Parameter Pipeline. II. Validation with Galactic Globular and Open Clusters, *AJ*, 136, 2050
- Lee, Y. S., Beers, T. C., Allende Prieto, C., et al. 2011a, The SEGUE Stellar Parameter Pipeline. V. Estimation of Alpha-element Abundance Ratios from Low-resolution SDSS/SEGUE Stellar Spectra, *AJ*, 141, 90
- Lee, Y. S., Beers, T. C., An, D., et al. 2011b, Formation and Evolution of the Disk System of the Milky Way:  $[\alpha/\text{Fe}]$  Ratios and Kinematics of the SEGUE G-Dwarf Sample, *ApJ*, 738, 187
- Lee, Y. S., Beers, T. C., Masseron, T., et al. 2013, Carbon-enhanced Metal-poor Stars in SDSS/SEGUE. I. Carbon Abundance Estimation and Frequency of CEMP Stars, *AJ*, 146, 132
- Lee, Y. S., Suda, T., Beers, T. C., & Stancliffe, R. J. 2014, Carbon-Enhanced Metal-Poor Stars in SDSS/SEGUE. II. Comparison OF CEMP-Star Frequencies with Binary Populations-Synthesis Models, *ApJ*, 788, 131
- Lee, Y. S., Beers, T. C., Carlin, J. L., et al. 2015, Application of the SEGUE Stellar Parameter Pipeline to LAMOST Stellar Spectra, *AJ*, 150, 187
- Lee, Y. S., Beers, T. C., Kim, Y. K., et al. 2017, Chemical Cartography. I. A Carbonicity Map of the Galactic Halo, *ApJ*, 836, 91
- Lee, Y.-W., Kim, J. J., Johnson, C. I., et al. 2019, The Globular Cluster Origin of the Milky Way Outer Bulge: Evidence from Sodium Bimodality, *ApJL*, 878, L2
- Lim, D., Lee, Y.-W., Koch, A., et al. 2021, Difference in Chemical Composition between the Bright and Faint Red Clump Stars in the Milky Way Bulge, *ApJ*, 907, 47
- Lindgren, L., Klioner, S. A., Hernández, J., et al. 2021, Gaia Early Data Release 3. The astrometric solution, *A&A*, 649, A2

- Majewski, S. R., Nidever, D. L., Smith, V. V., et al. 2012, Exploring Halo Substructure with Giant Stars: Substructure in the Local Halo as Seen in the Grid Giant Star Survey Including Extended Tidal Debris from  $\omega$ Centauri, *ApJL*, 747, L37
- Majewski, S. R., Schiavon, R. P., Frinchaboy, P. M., et al. 2017, The Apache Point Observatory Galactic Evolution Experiment (APOGEE), *AJ*, 154, 94
- Martell, S. L., & Grebel, E. K. 2010, Light-element abundance variations in the Milky Way halo, *A&A*, 519, A14
- Martell, S. L., Smolinski, J. P., Beers, T. C., & Grebel, E. K. 2011, Building the Galactic halo from globular clusters: evidence from chemically unusual red giants, *A&A*, 534, A136
- Martell, S. L., Shetrone, M. D., Lucatello, S., et al. 2016, Chemical Tagging in the SDSS-III/APOGEE Survey: New Identifications of Halo Stars with Globular Cluster Origins, *ApJ*, 825, 146
- Massari, D., Koppelman, H. H., & Helmi, A. 2019, Origin of the system of globular clusters in the Milky Way, *A&A*, 630, L4
- McMillan, P. J. 2017, The mass distribution and gravitational potential of the Milky Way, *MNRAS*, 465, 76
- Milone, A. P., Marino, A. F., Piotto, G., et al. 2015, The Hubble Space Telescope UV Legacy Survey of galactic globular clusters - II. The seven stellar populations of NGC 7089 (M2)\*, *MNRAS*, 447, 927
- Myeong, G. C., Evans, N. W., Belokurov, V., Sanders, J. L., & Koposov, S. E. 2018, The Sausage Globular Clusters, *ApJL*, 863, L28
- Myeong, G. C., Vasiliev, E., Iorio, G., Evans, N. W., & Belokurov, V. 2019, Evidence for two early accretion events that built the Milky Way stellar halo, *MNRAS*, 488, 1235
- Myeong, G. C., Vasiliev, E., Aguado, D. S., et al. 2022, Milky Way's Eccentric Constituents with Gaia, APOGEE, and GALAH, *ApJ*, 938, 21
- Naidu, R. P., Conroy, C., Bonaca, A., et al. 2020, Evidence from the H3 Survey That the Stellar Halo Is Entirely Comprised of Substructure, *ApJ*, 901, 48
- Pancino, E., Romano, D., Tang, B., et al. 2017, The Gaia-ESO Survey. Mg-Al anti-correlation in iDR4 globular clusters, *A&A*, 601, A112
- Pereira, C. B., Smith, V. V., Drake, N. A., et al. 2017, Chemical abundances and kinematics of TYC 5619-109-1, *MNRAS*, 469, 774
- Pereira, C. B., Holanda, N., Drake, N. A., et al. 2019, Search for Sodium-rich Stars among Metal-poor Stars, *AJ*, 157, 70
- Pfeffer, J., Kruijssen, J. M. D., Crain, R. A., & Bastian, N. 2018, The E-MOSAICS project: simulating the formation and co-evolution of galaxies and their star cluster populations, *MNRAS*, 475, 4309
- Pfeffer, J., Bastian, N., Kruijssen, J. M. D., et al. 2019, Young star cluster populations in the E-MOSAICS simulations, *MNRAS*, 490, 1714
- Phillips, S. G., Schiavon, R. P., Mackereth, J. T., et al. 2022, APOGEE detection of N-rich stars in the tidal tails of Palomar 5, *MNRAS*, 510, 3727
- Piotto, G., Milone, A. P., Bedin, L. R., et al. 2015, The Hubble Space Telescope UV Legacy Survey of Galactic Globular Clusters. I. Overview of the Project and Detection of Multiple Stellar Populations, *AJ*, 149, 91
- Placco, V. M., Frebel, A., Beers, T. C., Stancliffe, R. J. 2014, Carbon-enhanced Metal-poor Star Frequencies in the Galaxy: Corrections for the Effect of Evolutionary Status on Carbon Abundances, *ApJ*, 797, 21
- Rockosi, C. M., Lee, Y. S., Morrison, H. L., et al. 2022, SEGUE-2: Old Milky Way Stars Near and Far, *ApJS*, 259, 60
- Rostami Shirazi, A., Haghi, H., Khalaj, P., Asl, A. F., & Hasani Zonoozi, A. 2022, The escape of globular clusters from the satellite dwarf galaxies of the milky way, *MNRAS*, 513, 3526
- Savino, A., & Posti, L. 2019, Gaia DR2 orbital properties for field stars with globular cluster-like CN band strengths, *A&A*, 624, L9
- Schiavon, R. P., Zamora, O., Carrera, R., et al. 2017a, Chemical tagging with APOGEE: discovery of a large population of N-rich stars in the inner Galaxy, *MNRAS*, 465, 501
- Schiavon, R. P., Johnson, J. A., Frinchaboy, P. M., et al. 2017b, APOGEE chemical abundances of globular cluster giants in the inner Galaxy, *MNRAS*, 466, 1010
- Schönrich, R., Binney, J., & Dehnen, W. 2010, Local kinematics and the local standard of rest, *MNRAS*, 403, 1829
- Smolinski, J. P., Lee, Y. S., Beers, T. C., et al. 2011, The SEGUE Stellar Parameter Pipeline. IV. Validation with an Extended Sample of Galactic Globular and Open Clusters, *AJ*, 141, 89
- Suda, T., Komiya, Y., Yamada, S., et al. 2013, Transition of the stellar initial mass function explored using binary population synthesis, *MNRAS*, 432, L46
- Tang, B., Fernández-Trincado, J. G., Liu, C., et al. 2020, On the Chemical and Kinematic Consistency between N-rich Metal-poor Field Stars and Enriched Populations in Globular Clusters, *ApJ*, 891, 28
- Tang, B., Wang, Y., Huang, R., et al. 2021, Multiple Populations in Low-mass Globular Clusters: Palomar 13, *ApJ*, 908, 220
- Thomas, G. F., Jensen, J., McConnachie, A., et al. 2020, The Hidden Past of M92: Detection and Characterization of a Newly Formed 17° Long Stellar Stream Using the Canada-France Imaging Survey, *ApJ*, 902, 89
- Vasiliev, E. 2019, Proper motions and dynamics of the Milky Way globular cluster system from Gaia DR2, *MNRAS*, 484, 2832
- Vasiliev, E., & Baumgardt, H. 2021, Gaia EDR3 view on galactic globular clusters, *MNRAS*, 505, 5978
- Wan, Z., Lewis, G. F., Li, T. S., et al. 2020, The tidal remnant of an unusually metal-poor globular cluster, *NATURE*, 583, 768
- Xiang, M., Ting, Y.-S., Rix, H.-W., et al. 2019, Abundance Estimates for 16 Elements in 6 Million Stars from LAMOST DR5 Low-Resolution Spectra, *ApJS*, 245, 34
- Yanny, B., Rockosi, C., Newberg, H. J., et al. 2009, SEGUE: A Spectroscopic Survey of 240,000 Stars with  $g = 14-20$ , *AJ*, 137, 4377
- York, D. G., Adelman, J., Anderson, J. E., et al. 2000, The Sloan Digital Sky Survey: Technical Summary, *AJ*, 120, 1579

**Table 1**  
List of IDs for N-rich Stars

ID	ID	ID
LAMOST J000007.71+450217.7	SDSS J084931.26+563045.4	SDSS J151021.91+505013.8
LAMOST J000019.59+533825.5	SDSS J095223.17+535436.3	SDSS J151443.23+060657.0
SDSS J000150.47+284510.7	SDSS J095836.19+421757.7	SDSS J151519.74+082851.5
LAMOST J000350.99+533248.5	SDSS J100419.85+025552.5	LAMOST J152413.93-021757.6
LAMOST J000459.21+490514.2	SDSS J100607.70+115538.8	SDSS J152624.59+503349.0
LAMOST J012016.08+533733.7	SDSS J100747.12+014348.6	SDSS J160327.57+173348.6
SDSS J012108.81+395314.7	SDSS J102826.26+175448.9	SDSS J160531.97+044031.1
LAMOST J012350.31+570326.5	SDSS J104005.94+454033.9	SDSS J160709.23+044712.7
SDSS J014236.78-091334.8	SDSS J104730.17+221139.1	SDSS J160743.57+055029.2
SDSS J014604.43+142639.4	SDSS J104928.34+472825.1	SDSS J161535.29+311750.0
SDSS J022754.91+231139.6	SDSS J105403.30+482802.1	LAMOST J161746.22+242527.3
SDSS J023303.33+230841.3	SDSS J105843.49+152902.5	SDSS J164715.46+341627.5
LAMOST J023724.85+393802.9	SDSS J111406.40+404741.2	LAMOST J164736.87-054159.8
LAMOST J024634.61+392504.3	SDSS J112602.86-074026.6	SDSS J165513.24+420300.2
SDSS J024857.28+011442.0	SDSS J113026.47-004127.4	SDSS J165540.67+114924.1
SDSS J025402.11-000718.8	SDSS J114443.02+073005.1	SDSS J165758.38+291440.4
SDSS J025933.62+382457.3	SDSS J120101.27+125047.6	SDSS J165818.11+210330.1
SDSS J031118.42+053248.2	SDSS J120321.15+134836.1	LAMOST J170657.57+320645.1
SDSS J031358.15+174232.9	SDSS J120836.77+391054.9	SDSS J172556.84+081101.8
LAMOST J033341.67+295134.2	SDSS J121024.09-011051.9	SDSS J172615.14+334012.6
LAMOST J041612.46+505937.3	SDSS J121226.54+210123.1	SDSS J173052.92+333303.1
LAMOST J042244.82+421623.6	SDSS J121228.73+105512.0	SDSS J173706.90+334120.3
SDSS J044209.56+220126.6	SDSS J122428.12+045337.0	SDSS J174257.32+245017.3
LAMOST J045052.80+481849.6	SDSS J123055.37+003428.2	LAMOST J174842.61+225103.7
SDSS J050358.50-035445.5	SDSS J123205.79+243911.2	LAMOST J180132.38+072643.4
LAMOST J052018.92+362128.4	SDSS J124829.56+290621.9	SDSS J181146.33+242210.7
LAMOST J052730.80+175343.4	SDSS J125030.95+094751.7	SDSS J183725.43+411133.3
LAMOST J053109.08+501417.5	SDSS J125249.85-013746.8	SDSS J184947.27+183643.2
LAMOST J053119.44+183419.5	SDSS J125311.24+103948.8	SDSS J192123.01+615917.8
LAMOST J053158.79+193844.3	SDSS J130017.60+203702.4	SDSS J200837.14-103618.6
LAMOST J060742.47-034804.1	SDSS J130224.56+294930.1	SDSS J204914.05+003145.0
LAMOST J061423.84+325649.6	SDSS J130348.68+502648.1	SDSS J211830.64-062007.0
LAMOST J061955.84+023338.1	LAMOST J130953.85-012145.2	SDSS J211957.83-055835.8
LAMOST J063206.58+205410.4	SDSS J131958.14-001551.9	SDSS J221334.14-072604.1
LAMOST J064124.29+274954.1	SDSS J132109.65+412929.2	SDSS J223752.75+131427.6
LAMOST J064348.15+250115.2	SDSS J132443.92+542751.2	SDSS J223825.62+142623.3
LAMOST J064859.92+432420.9	SDSS J134143.89+282931.0	SDSS J224955.06+312228.8
LAMOST J072050.58+044121.7	SDSS J134245.48+282445.3	SDSS J233305.69+004541.5
SDSS J072157.19+381756.7	SDSS J134612.66+464651.1	LAMOST J233520.88+352011.6
SDSS J073136.00+165109.6	SDSS J140849.44+535803.5	SDSS J233703.57+084740.2
LAMOST J080417.90+060550.6	SDSS J145121.97+401638.9	SDSS J233906.83+073805.4
SDSS J080735.71+071805.4	SDSS J145134.72+415036.4	SDSS J233942.28+141615.6
LAMOST J081214.46+030750.8	SDSS J145320.16+094750.3	SDSS J234033.39+152620.4
SDSS J081344.87+662517.4	SDSS J145500.26+235832.0	SDSS J234323.62-093251.7
SDSS J083935.93+560913.7	SDSS J145613.98-000906.9	SDSS J234425.60-101739.1
SDSS J084032.28+221825.9	SDSS J150721.66+454006.8	SDSS J235238.21+140745.1